Chapter

# Conductive Effect of Increased Crystallinity of Single-Walled Carbon Nanotubes as Field Emitter

*Norihiro Shimoi*

## Abstract

Carbon nanotubes (CNTs) exhibit chemical stability, thermal conductivity, mechanical strength, and unique properties as a quasi-one-dimensional material with nanoscale needle shape. Field-emission (FE) electron sources appear to be the most promising industrial application for CNTs, and their deployment is approaching practical utilization. So far, efforts to construct an FE cathode with single-walled carbon nanotubes (SWCNTs) have only managed to average out the large FE current fluctuations in a nonhomogeneous electron emitter plane and the short emission lifetime because the crystal defects in the carbon network in CNTs prevent the realization of a stable emission current. The utilization of CNTs to obtain an effective electronic device, one with stable emission and low FE current fluctuations, relies on the high crystallization of CNTs, a task that can be fulfilled by using highly crystalline SWCNTs (hc-SWCNTs). The author could succeed in developing a model of the flow of electrons through the inside of the hc-SWCNTs and SWCNTs with crystal defects to the outside using the fluctuations of the tunneling current. Therefore, we expect that the hc-SWCNTs are used as field emitters with stable emission and low power consumption for saving energy.

**Keywords:** single-walled carbon nanotube, high crystallization, field emission, inelastic electron tunneling, current fluctuation

## 1. Introduction

In the development regime of electronic devices, carbon nanotubes (CNTs) are expected to represent a promising material because of their unique physicochemical properties—nanoscale needle shape, high chemical stability, thermal conductivity, and mechanical strength—which represent advantages for the fabrication of field emitters. The utilization of single-walled CNTs (SWCNTs) relies on their electronic properties because they can be either metallic or semimetallic, depending on the geometry of how a graphene sheet is rolled into a tube (i.e., diameter and chiral angle) [1–3]. This controllability is considered to be effective for developing electronic devices based on SWCNTs [3–5]. SWCNTs also exhibit one-dimensional confinement effects and can be used as coherent quantum wires [6–8], and the Young's modulus of SWCNTs is especially high when compared to that of other

CNTs [9]. Owing to these properties, SWCNTs have been used in a wide range of applications including field emitters [10], probes in scanning microscopes [11], gas-storage materials [12], and electrode materials for secondary batteries [13], and they have been studied in a wide range of applied research fields.

However, synthesized CNTs, including SWCNTs, have crystal defects in the carbon network, and the unstable physicochemical properties make it difficult to use CNTs in electronic devices which require high reliability. Tohji et al. improved the purity and crystallinity of SWCNTs synthesized by arc discharge, and they succeeded in obtaining highly pure SWCNTs [14]. Together with Iwata and coworkers, they established a method to analyze, with high resolution, the crystallinity of highly crystalline SWCNTs (hc-SWCNTs) [15]. Based on these developments, a process for synthesizing hc-CNTs has been gradually established; however, a technique to control the crystallinity of hc-SWCNTs has yet to be demonstrated.

The application of hc-SWCNTs as field emitters is industrially promising and is approaching practical utilization. We have carried out basic research to develop field-emission (FE) devices using hc-SWCNTs [16] and succeeded, for the first time in recorded history, in employing SWCNT field emitters as the cathode of a planar lighting device [17]. These results suggest that hc-SWCNTs will be indispensable for decreasing the driving voltage for FE, increasing the emission lifetime, and improving the homogeneity of planar emission of planar lighting devices [17].

In the chapter reported here, the effect of the increased crystallinity of SWCNTs on their electrical properties was examined by comparing hc-SWCNTs and SWCNTs with crystal defects. In addition, field emitters were prepared from these SWCNTs, and the effects of the increased crystallinity of hc-SWCNTs on their electrical conductivity and FE current fluctuations were theoretically analyzed by determining their FE properties.

## 2. Theoretical electron tunneling model of the increased conductivity of hc-SWCNTs as field emitters

The Fowler-Nordheim (F-N) tunneling model shown in **Figure 1** is an electron tunneling model represented by Eq. (1). The F-N tunneling model is valid only when electrons in the field emitter are passing into an energy barrier quantum mechanically. We assume that electrons emit from SWCNTs to the outside in case of the FE model discussed in this chapter, and we constructed an FE model including F-N tunneling model by combining the model of inelastic and elastic tunneling electrons passing through the inside of SWCNTs to the outside.

In the quantum electron-tunneling model, the states of the electrons before and after tunneling through an energy barrier can be estimated by considering the energy transfer. According to Laks and Mills [18], the current density $\hat{J}\left(\vec{x},t\right)$ in the current-current correlation $\left\langle \hat{J}\left(\vec{x},t\right)^{*}\hat{J}\left(\vec{x},t\right)\right\rangle$ can be expressed in the following form:

$$\hat{I}(t) = \int \mathrm{d}x_{\parallel}\hat{J}\left(\vec{x},t\right), \tag{1}$$

where $\hat{I}(t)$ is the quantum-mechanical tunneling-current operator and represents the current flow at time $t$. The normalization $P$ of the wave function $\psi\left(\vec{x},t\right)$ is expressed as the probability density of electrons in a quantum barrier as follows:

$$P(\vec{x},t) = \left|\psi(\vec{x},t)\right|^2 = \psi^*(\vec{x},t)\psi(\vec{x},t). \tag{2}$$

When an electron exists in a sphere $\Omega$,

$$\frac{\partial}{\partial t}\int_{\Omega} P(\vec{x},t)d\vec{x}$$

$$= \int_{\Omega}\left(\psi^*\frac{\delta\psi}{\delta t}\right)d\vec{x} \;\;=\frac{1}{i\hbar}\int_{\Omega}(\psi^*H\psi - \psi H\psi^*)d\vec{x} \tag{3}$$

$$=\frac{i\hbar}{2m}\int_{A}(\psi^*\nabla\psi - \psi\nabla\psi^*)d\vec{A}$$

When $S(\vec{x},t) \equiv \frac{\hbar}{2im}(\psi^*\nabla\psi - \psi\nabla\psi^*)$,

$$\frac{\partial}{\partial t}\int_{\Omega} P(\vec{x},t)d\vec{x} = -\int_{\Omega}\nabla S(\vec{x},t)d\vec{x}. \tag{4}$$

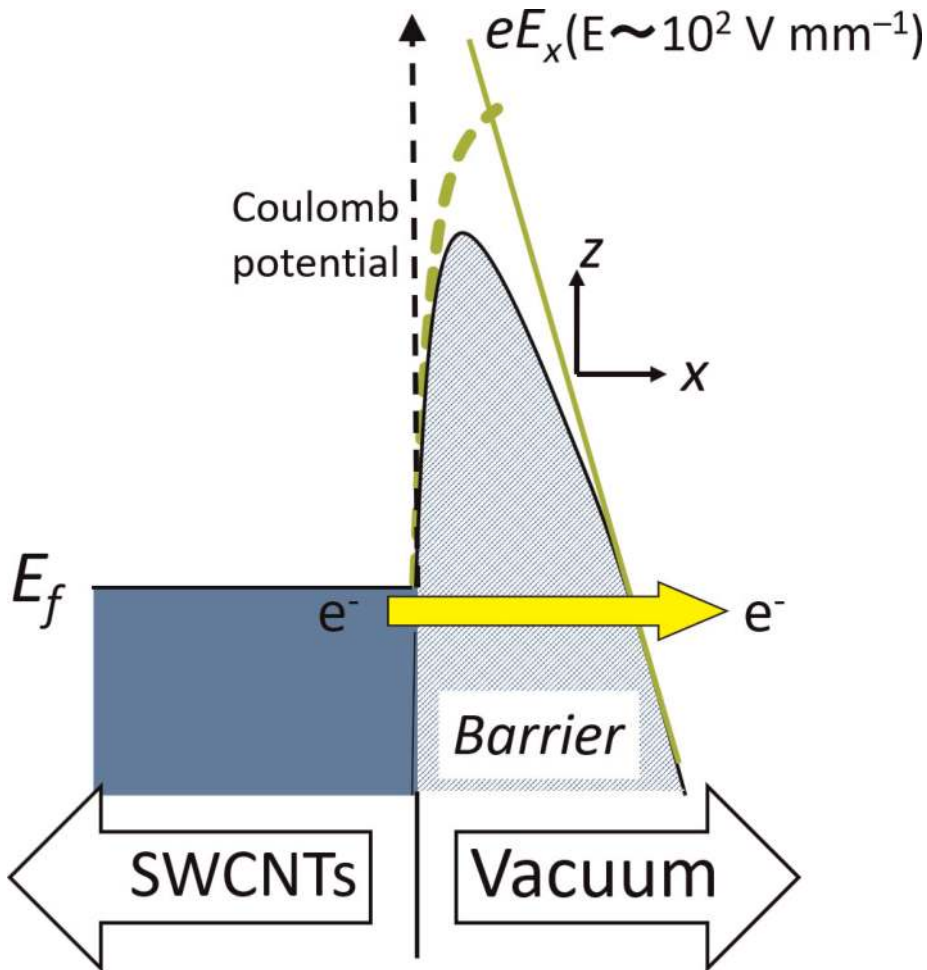When $\frac{\partial}{\partial t}P(\vec{x},t) + \nabla S(\vec{x},t) = 0$,



**Figure 1.**
*Schematic diagram of Fowler-Nordheim (F-N) tunneling.*

$$\hat{j}\left(\vec{x},t\right) = -e\hat{S}\left(\vec{x},t\right)$$

$$= \frac{ie\hbar}{2m}\left(\psi^*\nabla\psi - \psi\nabla\psi^*\right) \tag{5}$$

where $e$ is the electric charge. The quantum-mechanical tunneling-current operator $\hat{I}(t)$ can thus be expressed as:

$$\hat{I}(t) = \sum_{k \bullet q}\left[T_{kq}C_q^{r+}(t)C_k^l(t) + T_{kq}^*C_k^{l+}(t)C_q^r(t)\right], \tag{6}$$

where $T_{kq}$ is the tunneling matrix element between state $k$ of an electron in the SWCNT and state $q$ of an electron in the vacuum through a tunneling energy barrier, and $C_q^{r+}(t)$ and $C_k^l(t)$ are the creation and annihilation operators, respectively, of an electron before and after passing through an energy barrier. Using the Wentzel-Kramers-Brillouin (WKB) approximation to calculate the electron wave function, the tunneling matrix element can be expressed as [19–21]:

$$\left|T_{kq}\right| \propto \frac{\hbar^2}{2m^*}\exp\left(-\int_{z_1}^{z_r}dz\left|k_z(z)\right|\right)\exp\left(-\int_{z_1}^{z_r}dz\left|q_z(z)\right|\right), \tag{7}$$

where $m^*$ is the effective mass of the electron in the tunneling barrier, and $k_z$ and $q_z$ are the $z$ components of the electron wave vectors in the barrier perpendicular to the CNT surface:

$$k_z(z) = \frac{\sqrt{2m^*}}{\hbar}\left[V(z) - E + \frac{\hbar^2}{2m^*}k^2\right]^{\frac{1}{2}}, \tag{8}$$

$$q_z(z) = \frac{\sqrt{2m^*}}{\hbar}\left[V(z) - E + \frac{\hbar^2}{2m^*}k^2 + \hbar\omega\right]^{\frac{1}{2}}. \tag{9}$$

In Eqs. (8) and (9), $V(z)$ is the barrier potential, and $z$ is the coordinate of the axis perpendicular to the interfaces. The average of the current-current correlation in the $i^{\text{th}}$ state is expressed as follows:

$$\left\langle\hat{I}^*(t)\hat{I}(0)\right\rangle = \frac{1}{N}\sum_i\left\langle i\left|\hat{I}^*(t)\hat{I}(0)\right|i\right\rangle. \tag{10}$$

$|I(\omega)|^2$ is the power spectrum of the current fluctuation of the tunneling current for the field-emission mechanism:

$$|I(\omega)|^2 = \int_{-\infty}^{\infty}\left\langle\hat{I}^*(t)\hat{I}(0)\right\rangle\exp\left(-i\omega t\right)dt. \tag{11}$$

By substituting Eqs. (6)–(9) into Eq. (11), we can finally obtain the following expression for the power spectrum of the field-emission current fluctuations:

$$|I(\omega)|^2 = \frac{e^2Am}{2\pi^2\hbar^3}\int dE \times \exp\left(-\int dz\left|k_z(z)\right|\right)\exp\left(-\int dz\left|q_z(z)\right|\right), \tag{12}$$

where $A$ is the area of the field-emission site of the SWCNTs on a cathode, and $m$ is the effective mass of the electron that moves parallel to the emission site in the source electrode from which tunneling electrons are injected into the barrier.

Ballistic electrons are considered to pass through CNTs without crystal defects. However, when electrons pass through CNTs with crystal defects, the ballistic property is lost; an energy barrier is believed to inhibit the conduction of these electrons. In accordance with the works of Fransen et al. [22] and Nilsson et al. [23] on the electron tunneling model, we adopted an inelastic tunneling model through an energy barrier having a rectangular waveform.

## 2.1 Power spectrum in the inelastic tunneling model

In the inelastic tunneling model, the energy states of electrons passing through an energy barrier can be estimated by the energy transfer before and after electron tunneling. The power spectrum with the flow of FE current for the inelastic tunneling model was proposed by Kirtley et al. [24], Bardeen [25], and Watanabe et al. [26] based on Eqs. (12) and (13):

$$|I_{\text{in}}(\omega)|^2 \sim \int dE_{\parallel} \int dE_k \rho_k(E_k) \int dE_q \rho_q(E_q) |M_{kq}|^2 [(1 - n_q^{\text{r}})n_k^{\text{l}} - (1 - n_k^{\text{l}})n_q^{\text{r}}],$$

$$(13)$$

where $\rho(E)$ is the state density of electrons in one-dimensional space, and $n_i^{\text{h}}$ (h = l (for left region) or r (for right region)) is the occupation number of electrons within state $i$ ($i = k$ or $q$).

We attempted to obtain the direct-current (DC) component of the power spectrum of the inelastic electron tunneling model using a rectangular potential barrier and Eq. (13). As mentioned above, the electrons passing through the CNTs without crystal defects are ballistic [5]. The CNTs with crystal defects are reported to have an energy bandgap that depends on the position of the defects, and electrons rarely pass through CNTs without energy loss. In order to analyze the electrical conductivity of SWCNTs, we attempted to obtain the tunneling matrix $M_{kq}$ and the power spectrum of inelastic electron tunneling when electrons inelastically pass through the local area corresponding to crystal defects. The conductivity of electrons passing into SWCNTs with crystal defects was explained employing the electron tunneling model below.

For $M_{kq}$ of an energy barrier having a rectangular waveform, the state of wave function transfers that in the right region (r) to the left region (l) of the energy barrier or vice versa, $\varphi^r{}_q$ is the wave function having wavenumber $q$ localized in the right region of the barrier called as wave-B, and $\varphi^l{}_k$ is the wave function having wavenumber $k$ localized in the left region of the barrier called as wave-A. The Fermi level of an SWCNT is represented by $E_{\text{F}}$. When electrons pass through the rectangular potential barrier from the left region to the right region, the wave function shifts from state $k$ to state $q$, and the tunneling matrix $M_{kq}$ is given by:

$$M_{kq} = \int dx \left\{ \frac{\hbar^2}{2m} \nabla \varphi_k^{\text{l*}} \nabla \varphi_q^{\text{r}} + V(z) \varphi_k^{\text{l*}} \varphi_q^{\text{r}} \right\}, \qquad (14)$$

where $V(z)$ is the potential height of the energy barrier having a rectangular distribution on the $z$ axis shown in **Figure 2**, and $m$ is the effective mass of an electron.

The wave functions $\varphi_k$ and $\varphi_q$ localized in the left region (wave-A) and in the right region (wave-B) are represented by:

$$\varphi_k = \frac{1}{\sqrt{S}} e^{ik_{\parallel}|x||} \chi_k$$
$$, \qquad (15)$$
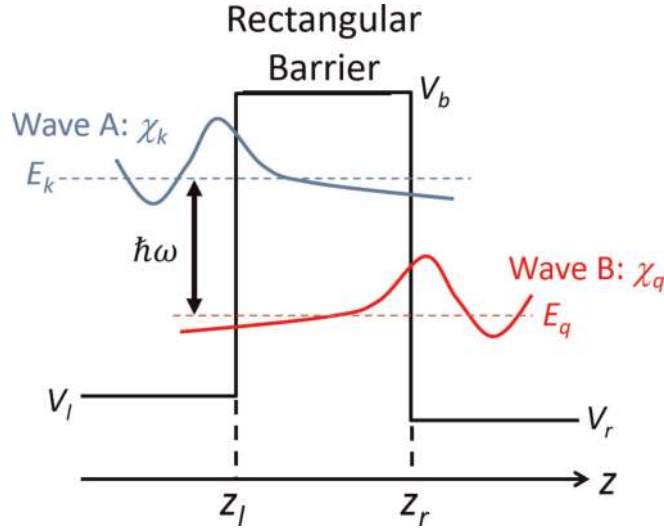$$\varphi_l = \frac{1}{\sqrt{S}} e^{iq_{\parallel}|x||} \chi_q$$

**Figure 2.**
*Image of a rectangular energy barrier having a potential height V(z).*

where $S$ is the area in which electrons pass through an SWCNT; and $k_\parallel$, $q_\parallel$, and $x_\parallel$ are the components, along the direction perpendicular to the $z$ axis, of the wavenumber $k$, wavenumber $q$, and position $x$, respectively. The wave functions $\chi_k$ and $\chi_q$ have coefficients $A_n$, $B_n$ and $C_n$, $D_n$, respectively, and are defined as:

$$
\begin{aligned}
\chi_k &= \sum_{n=l,\,b,\,r} \left( A_n e^{ik_n|z-z_n|} + B_j e^{-ik_n|z-z_n|} \right) \\
\chi_q &= \sum_{n=l,\,b,\,r} \left( C_n e^{iq_n|z-z_n|} + D_n e^{-iq_n|z-z_n|} \right)
\end{aligned}
\tag{16}
$$

The energy transfer between waves-A and -B, $\hbar\omega$, is included with the wavenumber in Eq. (16), and it corresponds to the energy loss of an electron passing through the energy barrier from the left region to the right region:

$$
\begin{aligned}
k_n &= \sqrt{\frac{\hbar^2}{2m}|E_z - V_n|}\,(n = l, b, r) \\
q_n &= \sqrt{\frac{\hbar^2}{2m}|E_z - V_n - \hbar\omega|}\,(z < z_l, z > z_r; n = l, r) \\
q_n &= \sqrt{\frac{\hbar^2}{2m}|E_z - V_n + \hbar\omega|}\,(z_l < z < z_r)
\end{aligned}
\tag{17}
$$

Using Eqs. (16) and (17), $M_{kq}$ can be rewritten as:

$$
M_{kq} \sim \delta_{k\|q\|} \sum_{n=l,\,b,\,r} \left[ \left( \frac{\hbar^2}{2m} k_n q_n - V_n \right) \frac{i}{k_n + q_n} \times \{A_n, B_n, C_n, D_n\} \right].
\tag{18}
$$

The power spectrum of inelastic electron tunneling, $|I_{\text{in}}(\omega)|^2$, is obtained from Eqs. (13)–(18). The power spectrum at $\omega = 0$ represents the magnitude of the direct current of the power spectrum $|I_{\text{in}}(\omega)|^2$.

## 2.2 Power spectrum in F-N tunneling regime passing into an SWCNT with crystal defect

The thickness of the rectangular energy barrier and the energy transfer which means the energy difference between the left region and the right region are
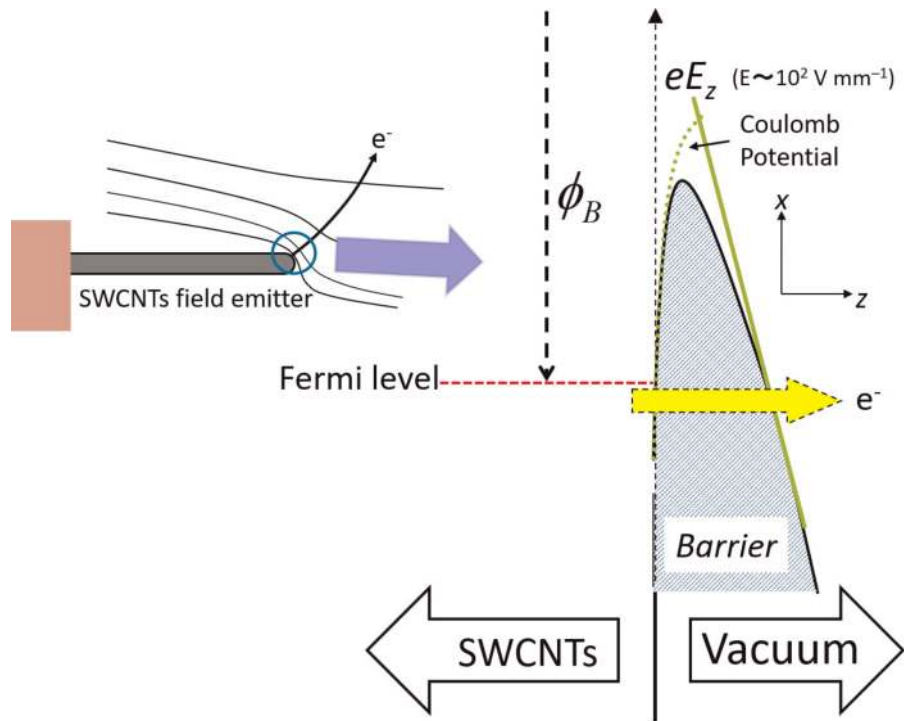
**Figure 3.**
*Original model of field emission using an SWCNT emitter in F-N tunneling.*

important factors in this simulation. Results of research on tunnel junction devices indicate that the thickness of the rectangular potential barrier for inelastic electron tunneling is only ~3 nm [20]. The energy loss caused by the tunneling of electrons through the energy barrier depends on the bandgap associated with the crystal defects [27]. The theoretical value of difference in the energy between waves A and B is calculated by fitting to be 0.027 eV, which corresponds to a temperature of 313 K for the energy loss observed when the electrons pass through SWCNTs with crystal defects.

Eq. (12) should be transformed into a more suitable form for a field-emission cathode using metallic SWCNTs. Field-emission measurements were carried out in the F-N tunneling regime, and a further simplified form is expressed as follows:

$$|I(\omega)|^2 \propto \frac{e^3 A}{4\pi^2 \hbar \phi_B} \bullet |E|^2 \left( \frac{\hbar\omega}{e\phi_B} + 1 \right)^{-1} \times \exp \left\{ -\frac{2\sqrt{2m}}{3\hbar e|E|} \left( (\hbar\omega)^{\frac{3}{2}} + (e\phi_B)^{\frac{3}{2}} \right) \right\}, \quad (19)$$

where $\phi_B$, shown in **Figure 3**, is the barrier-height potential that indicates the difference between the vacuum-level energy and the energy at the bottom of the Fermi level of metallic SWCNTs; and $E$ is the applied electric field on the SWCNTs enhanced by the tip shape. The enhancement factor $\beta$ of $E$ can be calculated by the surface-charge method of simulation using a three-dimensional SWCNT model that protrudes from an indium-tin oxide (ITO) film [28–30]:

$$E = \beta E_0, \quad (20)$$

where $E_0$ represents the real electric field between the cathode and anode. Moreover, the area of the field-emission site $A$ on the SWCNTs of the cathode was estimated from a comparison between the simulated and measured bright spots [30].

## 3. Experimental methods

In this study, the SWCNTs synthesized by arc discharge were annealed at a high temperature of approximately 1200 K in a low pressure of $10^{-6}$ Pa to obtain hc-SWCNTs. **Figure 4** shows transmission electron microscope (TEM) images of the SWCNTs before and after annealing. As shown in **Figure 4(a)**, we could find that the crystallinity of the SWCNTs after annealing was significantly improved.

The SWCNTs obtained before and after annealing were dispersed in a liquid medium with solvent including, to control the viscosity of the solution, surfactant and an ITO precursor solution, to prepare a coating film. The agitated mixture was sprayed on a silicon substrate to form an ITO film and sintered at approximately 700 K in a vacuum to remove any components in the organic solvents. In addition, to facilitate FE, the ITO film with SWCNTs was scratched with a thin needle to activate the film [16].

A diode structure fixed to the distance of 1.2 mm between a cathode of the ITO film having SWCNTs and an anode of a phosphor plate was prepared for the FE measurements; **Figure 5** shows a schematic of the FE-measurement system.
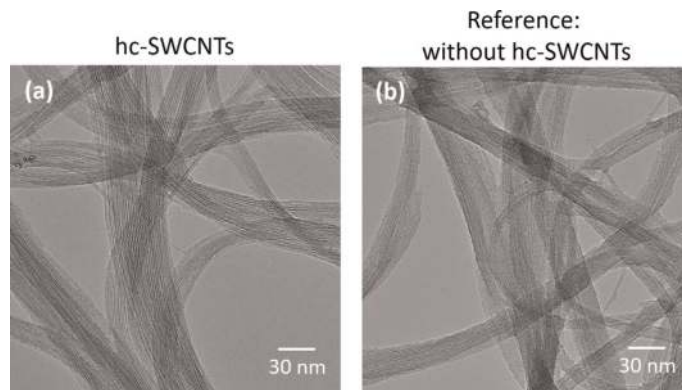


**Figure 4.**
*TEM images with annealed and unannealed SWCNTs: (a) annealed hc-SWCNTs; (b) nonannealed SWCNTs with crystal defects.*
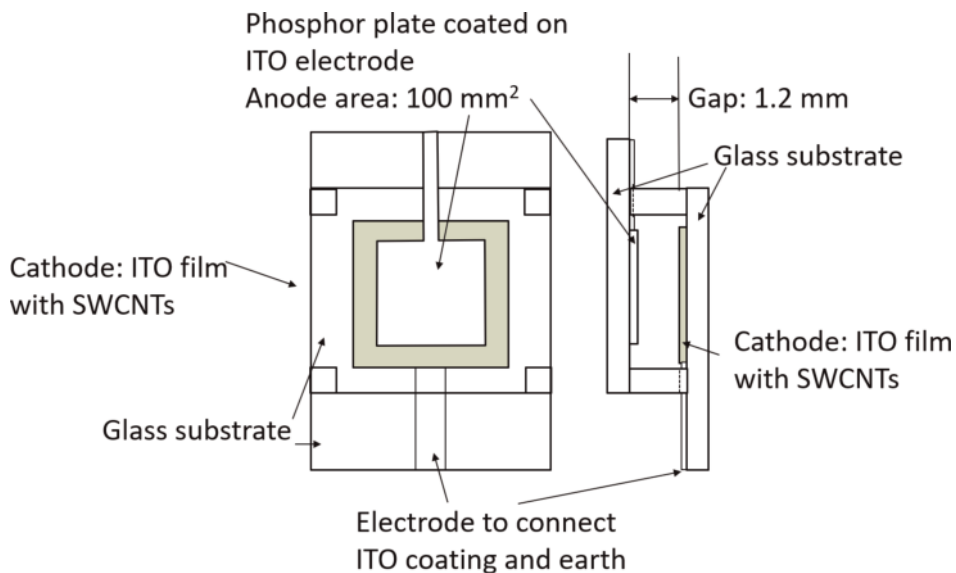


**Figure 5.**
*Schematic diagram of the FE-measurement system with a diode structure.*

The sample was set in a vacuum chamber of approx. $10^{-4}$ Pa. A supplied voltage with a frequency of 60 Hz was applied across the cathode and the anode to measure the FE characteristics.

## 4. Field-emission results and discussion

### 4.1 Field-emission characteristics of hc-SWCNTs

Tunneling electron microscopy and scanning electron microscopy were used to obtain images of the dispersed hc-SWCNT bundles and the ITO film which was subjected to activation treatment. As one can clearly see in the TEM image in **Figure 6(a)**, the hc-SWCNT bundles were well dispersed in the liquid medium. Meanwhile, the SWCNT bundles shown in the SEM image in **Figure 6(b)** were exposed in the scratched grooves on the activated ITO film and marked within the white circles; the dispersed SWCNTs in a scratched area are also illustrated with the red circles indicating the ends of the SWCNT bundles on the right. The number of dispersed and exposed SWCNTs per unit area could be controlled via the density of the SWCNTs. **Table 1** shows the summary of the state of the exposed SWCNTs in terms of (1) the number of SWCNTs protruding from the grooved walls of the scratched ITO film per unit area, (2) the mean diameter of the exposed SWCNT
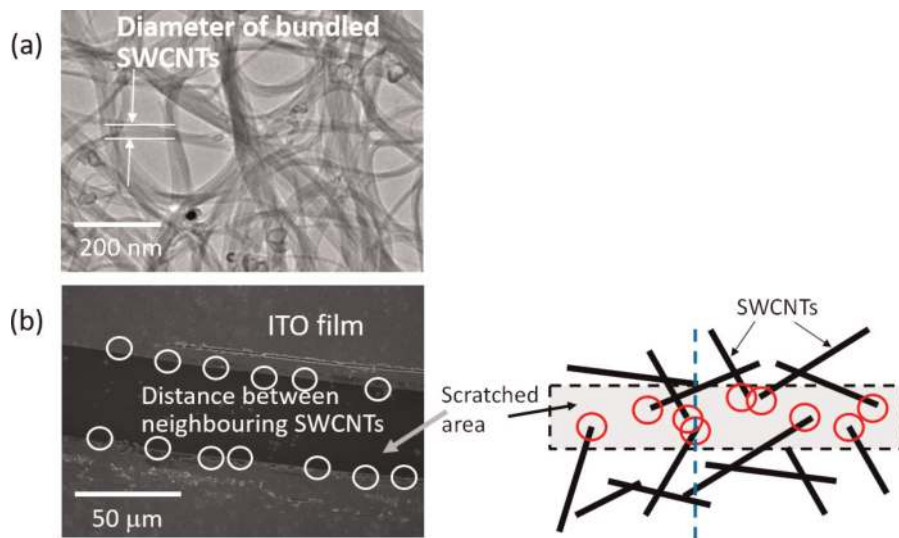


**Figure 6.**
*(a) TEM image of dispersed hc-SWCNT bundles. (b) Left: SEM image of scratched ITO film having SWCNTs, where the white circles show the SWCNT bundles protruding from the grooved walls of the ITO film; right: schematic diagram of scratched area including dispersed SWCNTs, where the red circles show the tops of the exposed SWCNTs in the scratched area.*

|  | hc-SWCNTs | SWCNTs with crystal defects |
|---|---|---|
| Number of SWCNTs exposed at grooved walls of ITO film after activation | Approx. 21 per $100 \times 100\ \mu m^2$ | Approx. 26 |
| Average diameter of bundled SWCNTs (nm) | Approx. 9 | Approx. 10 |
| Average distance between neighboring bundled SWCNTs (μm) | Approx. 27 | Approx. 21 |

**Table 1.**
*State of homogeneity of dispersed hc-SWCNTs and SWCNTs with crystal defects.*

bundles, and (3) the mean distance between neighboring SWCNT bundles for two types of SWCNTs, i.e., SWCNTs with crystal defects and hc-SWCNTs. The states of exposure of the two types of SWCNTs fabricated by our wet-coating process were similar, and they were homogeneously dispersed in the films.

**Figure 7** shows the relationship between the current density and electric field for the SWCNTs, obtained using the system for FE measurements (**Figure 5**). The threshold field decreased from 2.01 V μm$^{-1}$ for the SWCNTs with crystal defects to 1.07 V μm$^{-1}$ for the hc-SWCNTs. As shown in **Table 1**, the dispersion density of SWCNTs and the mean diameter of SWCNT bundles in the films were similar for the two types of the SWCNTs. It means that the probability densities of SWCNTs that induced FE were similar for the two types of SWCNTs. Therefore, it can be discussed and assumed that the above improvement in electrical properties was caused by the increase in crystallinity of the SWCNTs.

**Figure 8** shows the distribution of bright spots in the hc-SWCNTs and SWCNTs with crystal defects. As can be seen in **Figure 7**, the threshold and the driving field depended on the crystallinity of the SWCNTs. When the applied field was controlled so that the current density was uniform, the densities of the high- and low-brightness spots on the measured area were almost the same between the
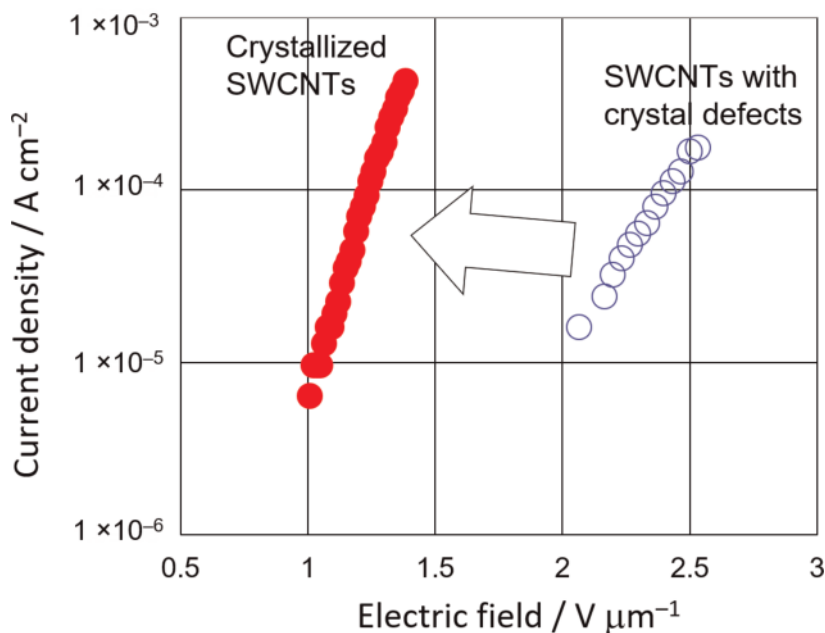


**Figure 7.**
*Semilog plot of current density versus electric field for hc-SWCNTs and SWCNTs with crystal defects.*
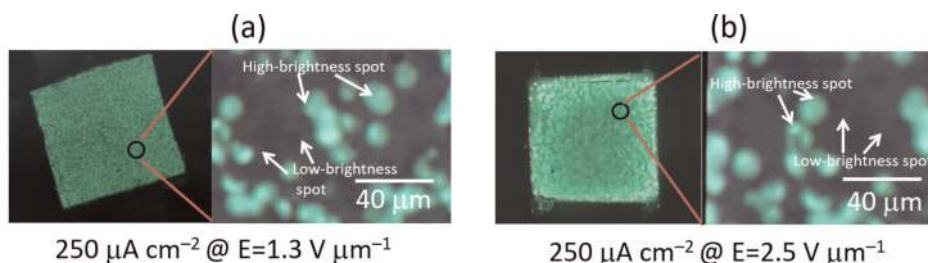


**Figure 8.**
*Homogeneity of emission sites homogeneity in (a) hc-SWCNTs and (b) SWCNTs with crystal defects. The panels on the left show planar lighting, and the enlarged view of the circled regions in the panels on the right show the distribution of spots of cathodes employing hc-SWCNTs and SWCNTs with crystal defects.*

hc-SWCNTs and the SWCNTs with crystal defects, respectively. Previous reports showed that in the SWCNTs synthesized by arc discharge, SWCNTs with metallic and semiconductive properties coexisted [31]. Therefore, the high-brightness spots can be attributed to the FE from metallic SWCNTs, and the low-brightness spots can be attributed to the FE from semiconductive SWCNTs; these phenomena and their origins are not discussed in this chapter. When the crystallinity of SWCNTs increased, the chirality of the carbon sheets making up the SWCNTs did not change, and the mixed ratio of metallic to semiconductive SWCNTs remained unchanged [32–37].

The results in **Figure 6** and **Table 1** indicate that the diameter, protruded length, and dispersion density of the SWCNT bundles protruding from the grooved ITO film were similar for the two types of the SWCNTs as FE electron sources. However, the difference in the plots of current density versus electric field of **Figure 7** is impossible to be analyzed only by the exposed uniformity of the dispersed SWCNTs on the activated ITO film. Therefore, we surmised that the difference in the crystallinity of SWCNTs caused the difference in electric properties of SWCNTs. Fransen et al. and Nilsson et al. find that the interruption of carbon network of an SWCNT with crystal defects originates a local energy band that affects the electrical conductivity by scanning tunneling microscopy (STM) [22, 23]. On the basis of the above results, an electric-physical model in an SWCNT was developed from the inelastic electron tunneling model. Therefore, the energy difference originated by the energy bandgap yielding from the interruption of carbon network in an SWCNT with crystal defects is surmised to become an energy barrier which impedes the electrons pass through the SWCNT.

**Figure 9** shows the FE properties obtained by experiment in **Figure 7** and simulation. For the hc-SWCNTs, the results obtained by the experiment are represented by red circles and those obtained by simulation using Eq. (12) at $\omega = 0$ of the F-N tunneling model without inelastic tunneling model are represented by the yellow dashed line. Moreover, the experimental results of the SWCNTs with crystal defects are represented by blue circles and those obtained by the following method are represented by the dark-red dashed line. We can find the fitting
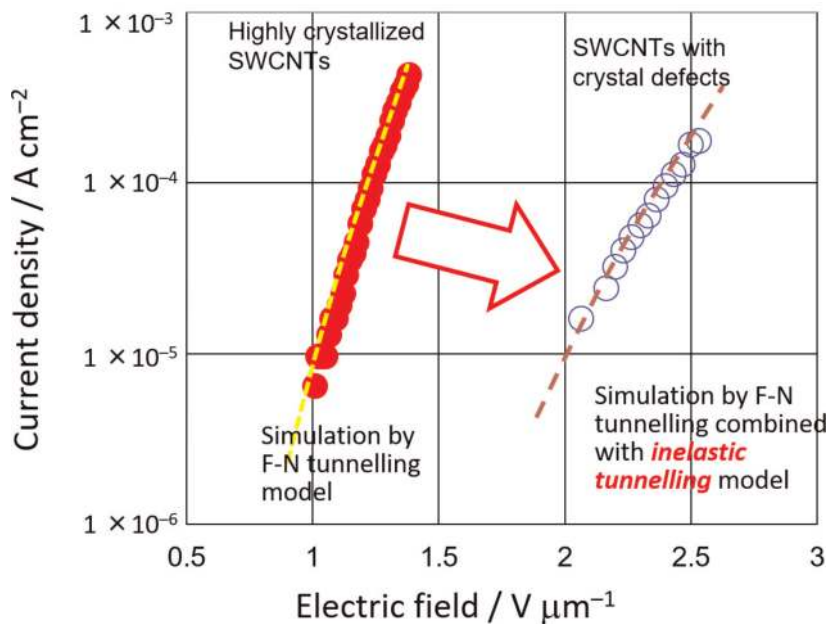


**Figure 9.**
*Fitting of simulation results to experimental current density-electrical field characteristics.*

|  | hc-SWCNTs | SWCNTs with crystal defects |
|---|---|---|
| Electron-emission site ($\alpha$) | | $1.95 \times 10^{-9}$ |
| Field-enhancement factor ($\beta$) | | 259,500 |
| Effective mass of electron ($m$) | | $1.00m_0$ ($m_0 = 9.11 \times 10^{-31}$ kg) |
| Thickness of rectangular inelastic barrier | — | 2.9 nm |
| Energy bandgap after passing into the barrier | — | 0.148 eV |
| Energy difference between wave A and wave B | — | 0.025 eV |

**Table 2.**
*Homogeneity of dispersed hc-SWCNTs and SWCNTs with crystal defects.*

between experiment and simulation is in good agreement. The simulation results represented by the dark-red dashed line were obtained by combining the F-N tunneling model of electrons emitted from the end of the SWCNT with the power spectrum with inelastic tunneling model given by Eqs. (7)–(12) at $\omega = 0$. **Table 2** shows the summary of the parameters employed in the theoretical calculations on the basis of F-N tunneling and inelastic electron tunneling. The total electron emission site area ($\alpha$) and the field-enhancement factor ($\beta$) for FE are important parameters in evaluating the FE characteristics. These two parameters were the same for the two types of the SWCNTs.

The inelastic electron tunneling through the SWCNTs with crystal defects, as shown in **Figure 10**, is a phenomenon based on the energy loss associated with the electron transfer in the SWCNTs. Although many researchers have reported that CNTs exhibit ballistic electrical conductivity, such property has not been demonstrated in any experiment that we know of. We can express successfully the first
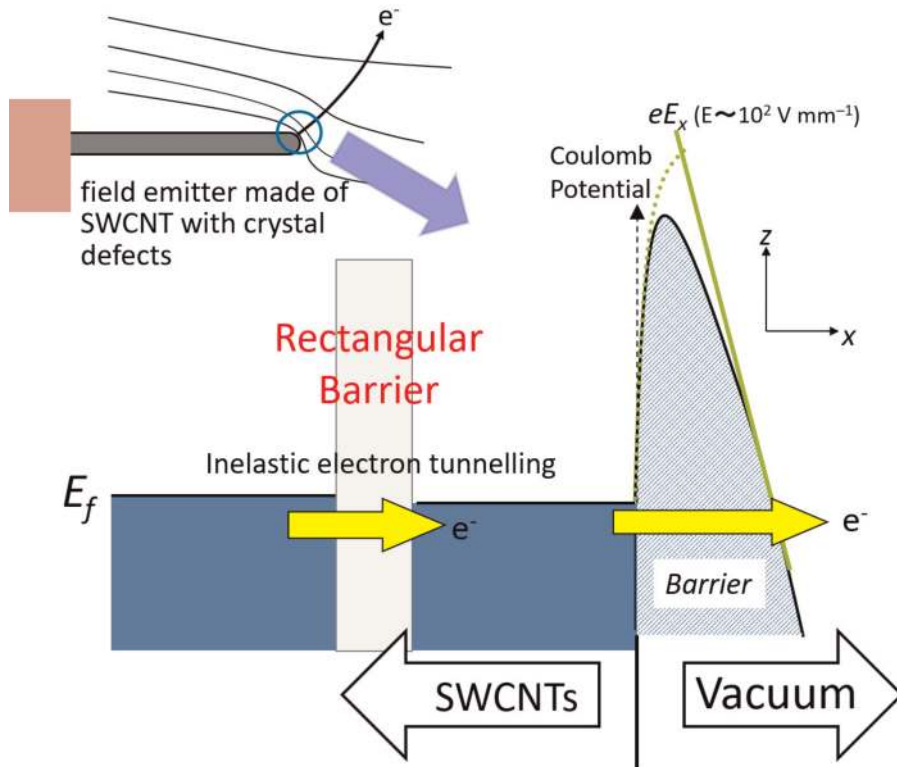


**Figure 10.**
*Schematic of field-emission property of SWCNTs with crystal defects modeled as convoluted FN-tunneling with inelastic tunneling.*

report of the development using an inelastic electron tunneling model for an SWCNT with crystal defects based on the evaluation of FE properties. The hc-SWCNTs are suitable materials for electronic devices to save energy because the energy loss associated with electron transfer in the SWCNT is suppressed.

### 4.2 Current fluctuations of hc-SWCNTs as field emitters: theoretical predictions versus experimental results

**Figure 11** shows the relationship between the current density and electric field for the SWCNTs obtained using the FE-measurement system shown in **Figure 5**. The threshold field of the metallic SWCNTs was 4.1 V $\mu m^{-1}$ at a line-current density of 0.1 mA $cm^{-2}$, as shown in **Figure 11**. Moreover, the planar lighting observed at 2 mA $cm^{-2}$ was homogeneous, as shown in the inset in **Figure 11**.

**Figure 12(a)** shows the stability of the FE current of metallic SWCNTs when different values of DC voltage were supplied for 50 s; **Figure 12(b)** shows the power spectrum of the frequency based on the FE current fluctuations by Fourier transform calculation. The current density obtained from the sample biased using the DC power supply was measured as 1.2 mA $cm^{-2}$ at 6 kV, 2.0 mA $cm^{-2}$ at 6.6 kV, 4.6 mA $cm^{-2}$ at 7.1 kV, and 10 mA $cm^{-2}$ at 7.6 kV. The FE current fluctuations were observed to be stable owing to the desorption of gases from the SWCNT surface caused by annealing before the FE measurements. Some damped current distributions in the FE current were expected if the annealing of the sample was insufficient. However, **Figure 12(a)** shows no damping, and the SWCNT surfaces were expected to be clean for the FE measurements. The spectrum of each FE current in **Figure 12(a)** is normalized by the peak at 0 Hz, and it indicates that periodic fluctuations were recorded. A peak appears at 50 Hz, as shown in **Figure 12(b)**, and it originated from the noise of the DC power supply, which represents the frequency of the commercial power supply in the eastern region in Japan. It can be seen that the stable DC current had alternating values, especially in the
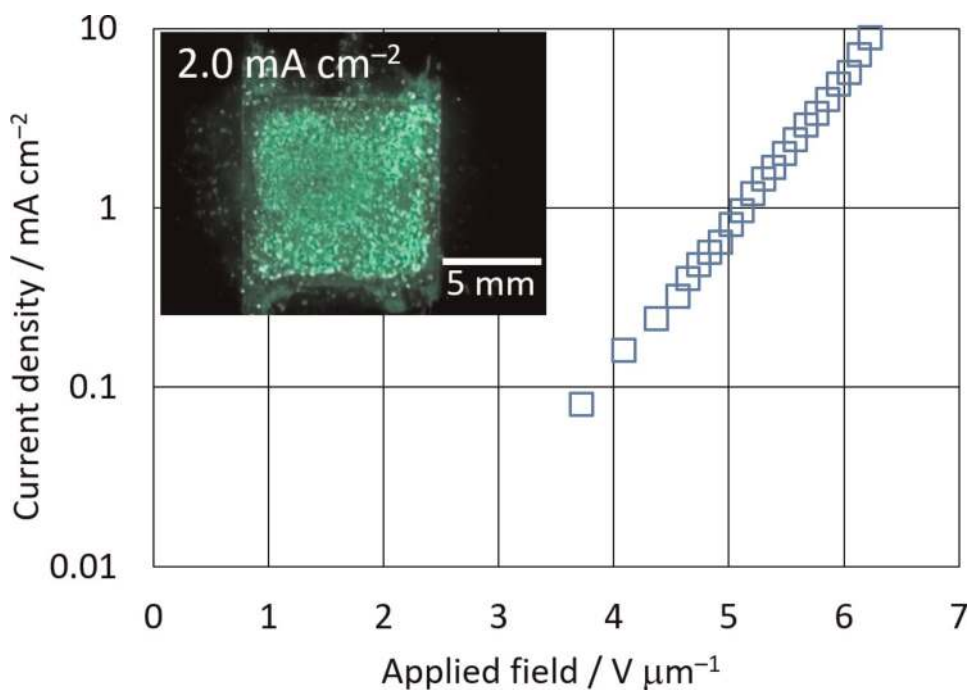


**Figure 11.**
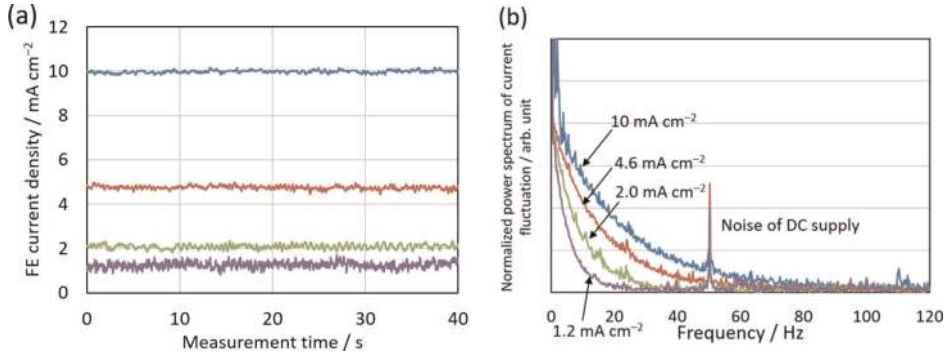*Current density-electric field characteristics of metallic SWCNTs; the inset shows the case of planar emission.*

**Figure 12.**
*(a) FE current fluctuations and (b) power spectra of FE-current fluctuations obtained by Fourier transform.*

| | |
|---|---|
| *e* (elementary charge) | $1.60 \times 10^{-19}$ C |
| *A* (area of field-emission site) | $6.48 \times 10^{-24}$ m$^2$ |
| $\phi_B$ (work function of bulk carbon) | 4.3 eV |
| $\hbar$ ($= \frac{h}{2\pi}$, *h*: Planck's constant) | $6.58 \times 10^{-16}$ eV s |
| $\beta$ (enhancement factor) | $2.56 \times 10^3$ |
| *m* (free electron mass) | $9.11 \times 10^{-31}$ kg |
| *A* and *β* were obtained from the simulation reported in Ref. [28]. | |

**Table 3.**
*Parameters used in the theoretical calculations.*

low-frequency domain of <100 Hz. Moreover, the spectrum distribution depends on the FE current, and the contents of each spectrum increased with the DC power.

When the experimental results and the theoretical predictions explained in the previous theoretical section are compared, the parameters that determined the tunneling characteristics of the metallic hc-SWCNTs used as field emitters are listed in **Table 3**. The enhanced field *E* in Eq. (20) was determined from the surface potential calculations with an SWCNT model. The area of the field-emission site, *A*, at the SWCNT surface was calculated from the analysis that determined the FE properties. Each SWCNT model protruded from the ITO wall, which included the minimum area for calculating the electric field using the surface-charge method. The potential parameter $\phi_B$ was estimated as the work function value of bulk carbon.

The power spectrum $|I(\omega)|^2$ obtained from Eq. (19) simplified by the WKB approximation shows the dependence of the applied field on a cathode using hc-SWCNTs, as shown in **Figure 13**. Each calculated spectrum was normalized, and it can be seen that $|I(\omega)|^2$ increased with the applied voltage at low frequency. For the metallic hc-SWCNTs, the experimental results are shown in **Figure 12**, and those obtained by simulation are shown in **Figure 13**; the two sets of results are in good agreement. From the above comment, the experimental results could be fitted well by the composition of the inelastic tunneling model and the F-N tunneling model employing the power spectrum of current fluctuation represented by Eq. (19). These results shown in **Figures 12** and **13** indicate that the electrons passing into a barrier in the F-N model exhibited the electron flow fluctuation in the inelastic tunneling model, and the shape of the power spectrum depended on the increased component of current fluctuation obtained from FE.
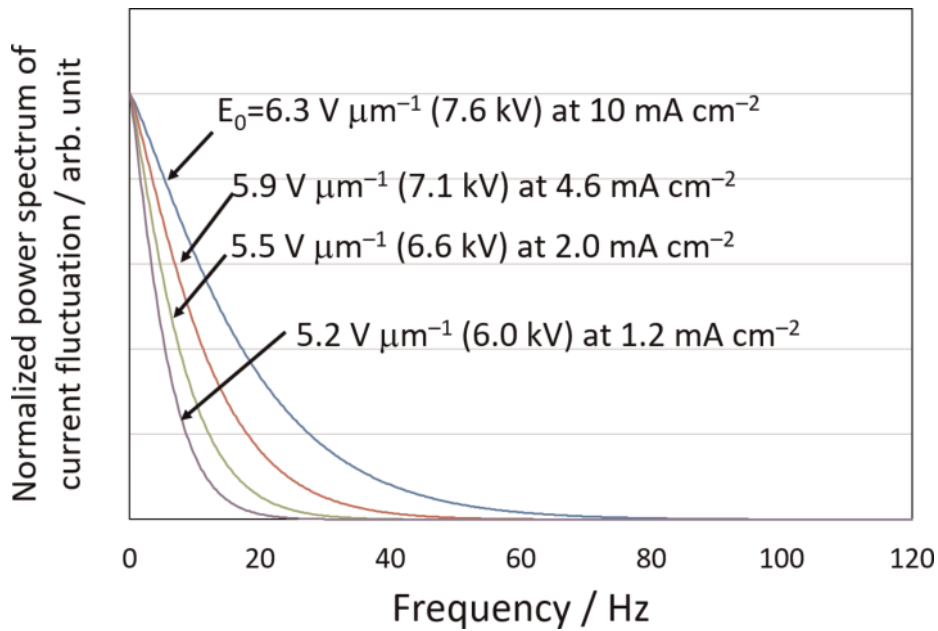
**Figure 13.**
*Power spectrum obtained by simulation showing the dependence on applied voltage; $E_o$ represents the original supplied electric field between the cathode and anode.*

Field emission using metallic SWCNTs was modeled as a phenomenon based on inelastic electron tunneling, and the calculated power spectra are shown in **Figure 13**. Although many researchers have reported that field emitters exhibit F-N tunneling with elastic electrical conductivity, the phenomenon has not been demonstrated in any reported experimental work. This chapter presents successfully the first report of the development of an inelastic electron-tunneling model with WKB approximation for SWCNTs from the FE properties. Moreover, the FE current from electron sources like SWCNTs contains time-depended fluctuations, and the *I-V* characteristics of the FE electron sources were expressed as the power spectrum at $\omega = 0$, which gives the magnitude of the current originating from the electrons passing through the SWCNTs, in accordance with the inelastic electron-tunneling model.

## 5. Conclusion

In this chapter, the author explained the conductive model of electrons flowing in the vicinity of a crystal defect that acts as a rectangular energy barrier based on inelastic electron tunneling model and the current fluctuation model for FE with hc-SWCNTs employing the F-N tunneling phenomenon.

The author could succeed in developing a model of the flow of electrons through the inside of an SWCNT to the outside using the fluctuations of the tunneling current. The electron flow model for an SWCNT with crystal defects was obtained by combining the F-N tunneling model with the power spectrum obtained using the tunneling matrix. From the previous mentioned comment, we could give a brief explanation of the effect of the increased crystallinity of SWCNTs on their electrical conductivity and describe the development of an electron flow model through the crystal defects of an SWCNT. Therefore, we expect that the hc-SWCNTs are used as field emitters with stable emission and low power consumption for saving energy.

## Acknowledgements

## Author details

Norihiro Shimoi
Graduate School of Environmental Studies, Tohoku University, Sendai, Japan

*Address all correspondence to: norihiro.shimoi.c8@tohoku.ac.jp

IntechOpen

# References

[1] Hamada N, Sawada S, Oshiyama A. New one-dimensional conductors: Graphitic microtubules. Physical Review Letters. 1992;**68**:1579-1581

[2] Saito R, Fujita M, Dresselhaus G, Dresselhaus MS. Electronic structure of chiral graphene tubules. Applied Physics Letters. 1992;**60**:2204-2206

[3] Tanaka K, Okahara K, Okada M, Yamabe T. Electronic properties of bucky-tube model. Chemical Physics Letters. 1992;**191**(5):469-472

[4] Kim J-Y, Kim M, Kim HM, Joo J, Choi J-H. Electrical and optical studies of organic light emitting devices using SWCNTs-polymer nanocomposites. Optical Materials. 2002;**21**:147-151

[5] Rinzler AG, Hafner JH, Nikolaev P, Lou L, Kim SG, Tomanek D, et al. Unraveling nanotubes: Field emission from an atomic nanowire. Science. 1995;**269**:1550-1553

[6] Ebbesen TW, Lezec HJ, Hiura H, Bennett JW, Ghaemi HF, Thio T. Electrical conductivity of individual carbon nanotubes. Nature. 1997;**382**:54-56

[7] Wildoerm JWG, Venema LC, Rinzler AG, Smalley RE, Dekker C. Electronic structure of atomically resolved carbon nanotubes. Nature. 1998;**391**:59-62

[8] Odom TW, Huang JL, Kim P, Lieber CM. Atomic structure and electronic properties of single-walled carbon nanotubes. Nature. 1998;**391**:62-64

[9] Treacy MMJ, Ebbesen TW, Gibson JM. Exceptionally high Young's modulus observed for individual carbon nanotubes. Nature. 1996;**381**:678-680

[10] Saito Y, Uemura S, Hamaguchi K. Cathode ray tube lighting elements with carbon nanotube field emitters. Japanese Journal of Applied Physics. 1998;**37**:L346-L348

[11] Dai H, Hafner JH, Rinzler AG, Colbert DT, Smalley RE. Nanotubes as nanoprobes in scanning probe microscopy. Nature. 1996;**384**:147-150

[12] Dillon AC, Jones KM, Bekkedahl TA, Kiang CH, Bethune DS, Haben MJ. Storage of hydrogen in single-walled carbon nanotubes. Nature. 1997;**386**:377-379

[13] Niu C, Sichel EK, Hoch R, Moy D, Tennent H. High power electrochemical capacitors based on carbon nanotube electrodes. Applied Physics Letters. 1997;**70**:1480-1482

[14] Tohji K, Goto T, Takahashi H, Shinoda Y, Shimizu N, Jeyadevan B, et al. Purifying single-walled nanotubes. Nature. 1996;**383**(6602):679-679

[15] Iwata S, Sato Y, Nakai K, Ogura S, Okano T, Namura M, et al. Novel method to evaluate the carbon network of single-walled carbon nanotubes by hydrogen physisorption. The Journal of Physical Chemistry Letters. 2007;**111**: 14937-14941

[16] Shimoi N, Adriana LE, Tanaka Y, et al. Properties of a field emission lighting plane employing highly crystalline single-walled carbon nanotubes fabricated by simple processes. Carbon. 2013;**65**:228-235

[17] Garrido SB, Shimoi N, Abe D, Hojo T, Tanaka Y, Tohji K. Planar light source using a phosphor screen with single-walled carbon nanotubes as field emitters. Review of Scientific Instruments. 2014;**85**:104704

[18] Laks B, Mills DL. Photon emission from slightly roughened tunnel junctions. Physical Review B. 1979;**20**: 4962-4980

[19] Watanabe J, Uehara Y, Ushioda S. Multiple-scattering effect of surface-plasmon polaritons in bright emission from tunnel junction. Physical Review B. 1995;**52**:2860-2867

[20] Uehara Y, Watanabe J, Fujikawa S, Ushioda S. Light-emission mechanism of Si-MOS tunnel junctions. Physical Review B. 1995;**51**:2229-2238

[21] Hone D, Muhlschlegel B, Scalapino DJ. Theory of light emission from small particle tunnel junctions. Applied Physics Letters. 1998;**33**:203-204

[22] Fransen MJ, van Rooy TL, Kruit P. Field emission energy distributions from individual multiwalled carbon nanotubes. Appl. Sur. Sci. 1999;**146**: 312-327

[23] Nilsson L, Groening O, Emmenegger C, Kuettel O, Schaller E, Schlapbach L. Scanning field emission from patterned carbon nanotube films. Applied Physics Letters. 2000;**76**: 2071-2073

[24] Kirtley JR, Theis TN, Tsang JC, DiMaria DJ. Hot-electron picture of light emission from tunnel junctions. Physical Review B. 1983;**27**:4601-4611

[25] Bardeen J. Tunneling from a many-particle point of view. Physical Review Letters. 1961;**6**:57-59

[26] Watanabe J, Uehara Y, Murota J, Ushioda S. Light emission from Si-metal-oxide-semiconductor tunnel junctions. Japanese Journal of Applied Physics, Part 1. 1993;**32**:99-101

[27] Shimoi N. Effect of increased crystallinity of single-walled carbon nanotubes used as field emitters on their electrical properties. Journal of Applied Physics. 2015;**118**:214304

[28] Murata H, Shimoyama H, Ohye T. Computer simulation of electric field analysis for vertically aligned carbon nanotubes: I. Simulation method and computing model. Proceedings of SPIE. 2001;**4510**:156-162

[29] Shimoyama H, Murata H, Ohye T. Computer simulation of electric field analysis for vertically aligned carbon nanotubes: II. Electric field on the nanotube apex. Proceedings of SPIE. 2001;**4510**:163-171

[30] Shimoi N, Tanaka S-I. Numerical analysis of electron emission site distribution of carbon nanofibers for field emission properties. ACS Applied Materials & Interfaces. 2012;**5**:768-773

[31] Wu B, Geng D, Liu Y. Evaluation of metallic and semiconducting single-walled carbon nanotube characteristics. Nanoscale. 2011;**3**:2074

[32] Saito Y, Hamaguchi K, Nishino T, Hata K, Tohji K, Kasuya A, et al. Field emission patterns from single-walled carbon nanotubes. Japanese Journal of Applied Physics. 1997;**36**:L1340-L1342

[33] Ren ZF, Huang ZP, Xu JW, Wang JH, Bush P, Siegal MP, et al. Synthesis of large arrays of well-aligned carbon nanotubes. Science. 1998;**282**:1105-1107

[34] Tsai SH, Chao CW, Lee CL, Shih HC. Bias-enhanced nucleation and growth of the aligned carbon nanotubes with open ends under microwave plasma synthesis. Applied Physics Letters. 1999;**74**:3462-3464

[35] Kim JM, Choi WB, Lee NS, Jung JE. Field emission from carbon nanotubes for displays. Diamond and Related Materials. 2000;**9**:1184-1189

[36] Popov VN. Carbon nanotubes: Properties and application. Materials Science and Engineering Reports. 2004; **43**:61-102

[37] Bandaru PR. Electrical properties and applications of carbon nanotube structure. Journal of Nanoscience and Nanotechnology. 2007;7:1239-1267